

Cao Xuan Cuong¹,
orcid.org/0000-0002-7405-9668,
Le Van Canh¹,
orcid.org/0000-0002-8113-9949,
Pham Van Chung¹,
orcid.org/0000-0002-6446-7860,
Le Duc Tinh¹,
orcid.org/0000-0002-0022-3453,
Pham Trung Dung¹,
orcid.org/0000-0002-9474-3723,
Ngo Sy Cuong²,
orcid.org/0000-0002-9466-7564

1 – Hanoi University of Mining and Geology, Hanoi, the Socialist Republic of Vietnam, e-mail: caoxuancuong@humg.edu.vn
2 – Vietnam Natural Resources and Environment Corporation, Hanoi, the Socialist Republic of Vietnam

QUALITY ASSESSMENT OF 3D POINT CLOUD OF INDUSTRIAL BUILDINGS FROM IMAGERY ACQUIRED BY OBLIQUE AND NADIR UAV FLIGHTS

Purpose. The main objective of this paper is to assess the quality of the 3D model of industrial buildings generated from Unmanned Aerial Vehicle (UAV) imagery datasets, including nadir (N), oblique (O), and Nadir and Oblique (N+O) UAV datasets.

Methodology. The quality of a 3D model is defined by the accuracy and density of point clouds created from UAV images. For this purpose, the UAV was deployed to acquire images with both O and N flight modes over an industrial mining area containing a mine shaft tower, factory housing and office buildings. The quality assessment was conducted for the 3D point cloud model of three main objects such as roofs, facades, and ground surfaces using CheckPoints (CPs) and terrestrial laser scanning (TLS) point clouds as the reference datasets. The Root Mean Square Errors (RMSE) were calculated using CP coordinates, and cloud to cloud distances were computed using TLS point clouds, which were used for the accuracy assessment.

Findings. The results showed that the point cloud model generated by the N flight mode was the most accurate but least dense, whereas that of the O mode was the least accurate but most detailed level in comparison with the others. Also, the combination of O and N datasets takes advantages of individual mode as the point cloud's accuracy is higher than that of case O, and its density is much higher than that of case N. Therefore, it is optimal to build exceptional accurate and dense point clouds of buildings.

Originality. The paper provides a comparative analysis in quality of point cloud of roofs and facades generated from UAV photogrammetry for mining industrial buildings.

Practical value. Findings of the study can be used as references for both UAV survey practices and applications of UAV point cloud. The paper provides useful information for making UAV flight planning, or which UAV points should be integrated into TLS points to have the best point cloud.

Keywords: *UAV, Oblique, Nadir, 3D modelling, terrestrial laser scanning, quality assessment*

Introduction. A three-dimension (3D) map is defined as a computer representation of a 3-D integrated geo-data model with cartographic content [1]. 3D maps play nowadays an increasingly important role in planning, designing, operating, and managing urban areas, including cities, towns and industrial zones [2–4]. In order to build a 3D map, a Digital Terrain Modeling (DTM) of the area is necessarily generated. Also, all objects located in the mapping area are needed to be modeled in the 3D space.

To date, 3D mapping or modeling has received considerable attention from both scientists and managers. There have been many technologies involving 3D mapping ranging from traditional ground surveying such as total station and GNSS to a new generation of remote sensing technologies, including Laser Imaging Detection and Ranging (LIDAR) and UAV [5, 6]. While traditional methods can produce a high accuracy but a poor density level of datasets, LIDAR and UAV can offer reasonable/exceptional accuracy and high-density datasets [7]. In addition, both LIDAR and UAV can create clouds of millions of 3D points with exceptional accuracy at quick times, so they are more effective than the total station and GNSS [7]. However, while LIDAR technology is still high cost, especially for the highly temporal data collection, the availability of low-cost UAV systems allows it to become a common approach to 3D mapping of urban areas.

When the UAV photogrammetry is chosen as a method of data collection for 3D mapping, there are two common UAV flight modes regarding the angle of the camera axis, including

nadir and oblique. While using the former, the UAV camera captures images with its axis along the vertical direction; for the latter, the images are shot with the camera axis at an angle with respect to the vertical (a camera inclination angle). In general, a UAV survey is often conducted with the nadir mode, but for 3D mapping of objects with a large vertical dimension such as towers, buildings, the oblique mode is more popular [8–11]. However, in 3D mapping of a large area, a combination of the two modes is usually performed using the nadir mode with linear flight patterns covering the whole area and the oblique one with orbital flight patterns focusing on high and/or complex objects [12–14].

So far, there have been numerous works focusing on the influence of camera inclination angle on the accuracy of 3D modelling. Several studies focused on oblique camera angles ranging from 05 to 35° and 3D mapping natural objects such as a deglaciated terrain with layers of siltstone and fine-to-medium-grained sandstone [12], from 10 to 20° and 3D mapping rocks [15], from 20 to 30° and 3D mapping forests [16], from 25 to 30° and mapping a coastal cliff surface [15], from 45 to 65° and mapping a coastal erosion scarp [17]. Other works focused on the 3D high-level-of-detail reconstruction of historical architectures, such as using an oblique angle of 45° [18], and 90° [19] for 3D modeling of heritage buildings. Another work used a tilt angle of the camera of 45° to 3D mapping a large area of the French city, Bordeaux [20]. Overall, the camera axis angle in a 45–90° range is often chosen for 3D mapping buildings.

In 3D modeling buildings, there are three main objects that should be considered, including facades, roofs, and the ground surface surrounding buildings as they influence the

quality of building documentation. The analysis may centre on the quality of the 3D model containing the accuracy and the density of the point cloud model. In industrial regions, factory buildings are one of the main features of these areas. They are often built in large sizes, with industrial materials, flat roofs, jutting edges, and polished surfaces, and partly contribute to the architecture of the region. However, so far, not many UAV based mapping studies have provided any comparative analysis of the 3D model of factory buildings regarding the three above objects generated from the UAV-Structure from Motion (UAV-SfM). The homogeneity of surfaces of factory housing might be one of the error sources in the UAV based 3D mapping. In this study, the quality of 3D point cloud models of facades, roofs, and surrounding ground surfaces was examined. The study aims to compare the accuracy and density of point cloud models generated from three cases of UAV image blocks, including the nadir imagery (Case N), the oblique imagery (Case O), and the combined nadir and oblique imagery (Case N + O).

Study area and data collection. Study site. In this study, the ground area of the Nui Beo underground coal mine was selected as the study area. This area is located in Quang Ninh province, Vietnam. Its area is about 12 hectares and features 5–6 story buildings and two mineshaft towers (Fig. 1). The construction of the two mine shafts began in 2012 and was completed in 2016. The designed capacity of coal production is approximately two million tons of coal per year. According to the design, the primary shaft is dug from the elevation of 35 to –410 m, equipped with cages to transport coal. The secondary shaft is dug from the elevation of 35 to –370 m, equipped with cages for transporting people, equipment, and construction materials. On the ground, only the wall of office buildings is built with bricks, while all roofs and the walls of factory

buildings are built with metal materials. This industrial mining architecture is quite popular.

Survey equipment. For data collection in this study, three survey instruments, including a DJI Inspire 2 drone, a FARO FOCUS^{3D} X130 laser scanner, and a Leica FlexLine TS09 total station were employed. These instruments were technically checked and validated to be at the ready-to-use status.

The camera mounted on the drone is crucially important as it contributes to the accuracy of resulting 3D models directly. In this study, the UAV camera is a Zenmuse X4S with a CMOS 1" sensor, 24 MegaPixel, a focal length of 8.8 mm/F2.8-11, and a FOV of 84° (Fig. 2).

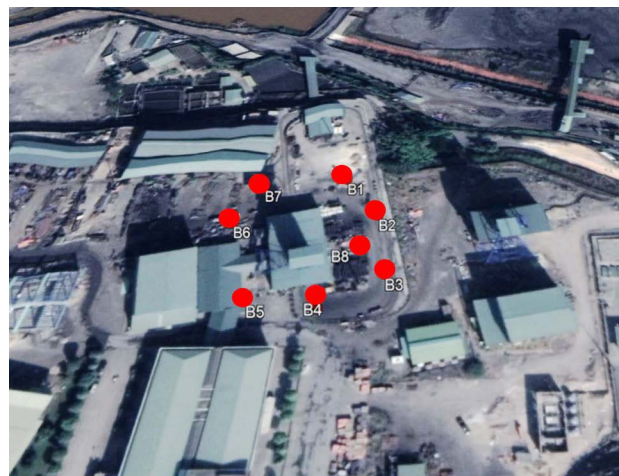
In order to evaluate the accuracy of 3D models generated from UAV, two assessment methods are using several checkpoints and dense point clouds. The acquisition of these reference datasets was performed using a Leica FlexLine TS09 total station and a FARO FOCUS^{3D} X130 laser scanner (Table 1).

Data collection. The data collection began with the measurement of ground control points (GCPs), checked points (CPs) and TLS targets in the VN-2000 coordinate system. The distribution of GCPs and CPs is shown in Fig. 3. There were 23 ground points measured by a Leica FlexLine TS09 (Table 1) with seven, four, and nine of them being used as CPs for the accuracy assessment of the nadir, oblique, and nadir and oblique cases, respectively (Figs. 3, a, b, c). The positional accuracy of these points was at the subcentimeter precision.

Several GCPs and CPs were chessboard markers placed on both ground surface and facades (Fig. 4). Their positions were measured using the Leica FlexLine TS09 total station in the non-prism mode for façade markers and the prism mode for ground markers. In addition to the purpose of georeferencing the TLS and UAV data, some of them were used for the alignment of UAV and TLS point clouds.



a



b

Fig. 1. Study area:

a – Industrial yard of an underground coal mine (within the yellow boundary line); b – TLS scan locations (red dots)



a





b

Fig. 2. UAV equipment:

a – DJI Inspire 2 drone; b – Zenmuse X4S camera

Table 1

Laser scanner and total station specifications

FARO FOCUS ^{3D} X130			
	Range of Measurement	90 % reflectivity	0.6–130 m
	Distance Accuracy		± 2 mm
	Scanning Rate (points/second)		Up to 976 000
	Field of View		360 × 300°
	Camera Resolution		70 MPixel
	Tilt Unit	Type	Dual axis compensator
Range		± 5°	
Leica FlexLine TS09			
	Angle measurement accuracy		1''
	Distance measurement accuracy	Prism	1.5 mm + 2 ppm
		Reflectorless	2 mm + 2 ppm

UAV flights for data collection were planned and operated using DJI GS Pro, a DJI UAV software installed on an Ipad. There were three flight plans, including one linear flight and two circular flights. While the linear flight plan was to acquire nadir images over the whole study area (Fig. 5, a), the circular one was to capture oblique images of the centre area with office buildings and the secondary mine shaft tower (Fig. 5, b).

Several important flight plan parameters were set up for each plan, such as flight height, image overlaps, camera optical axis angle. However, for circular flights, these parameters were extensive to flight radius and building radius, which are the distances from the centre of flight circular orbits to the drone and the boundary of focusing building. In addition, while the ground sample distance (GSD) of images is defined by the flight altitude in the linear flight mode, it is dependent on both the flight radius and altitude in the circular one. The drone was automatically operated in a stop-and-go mode, meaning the drone hovers before its camera shoots each image. This could, therefore, reduce negative impacts on the subsequent photogrammetric results. Table 2 compiles these important parameters and summarises the result of UAV data collection.

TLS survey was designed with eight external scans at the ground level (Fig. 1). Therefore, some parts of the second

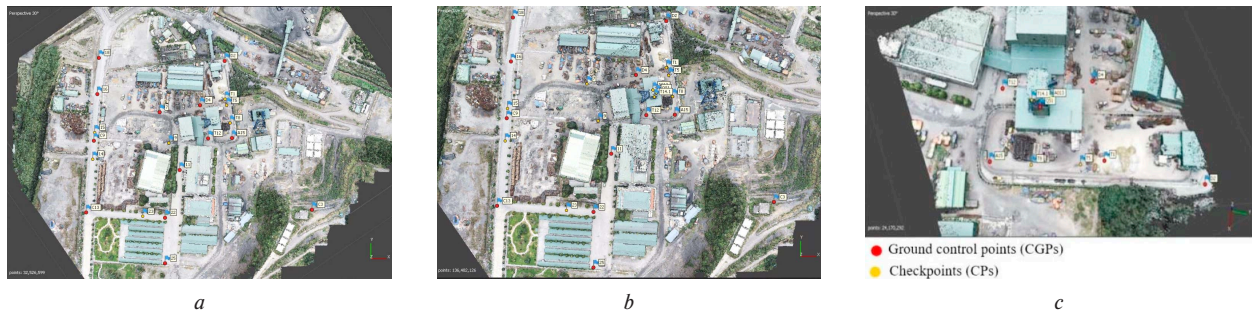


Fig. 3. Distribution of GCPs and CPs for:
a – the nadir; b – oblique; c – nadir and oblique cases

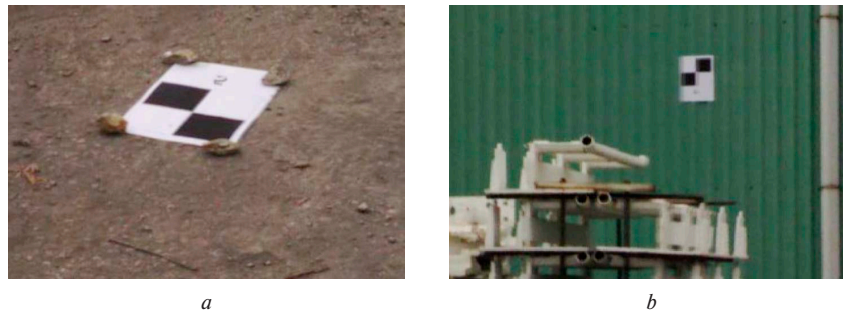


Fig. 4. Markers placed on (a) the ground and (b) the facade

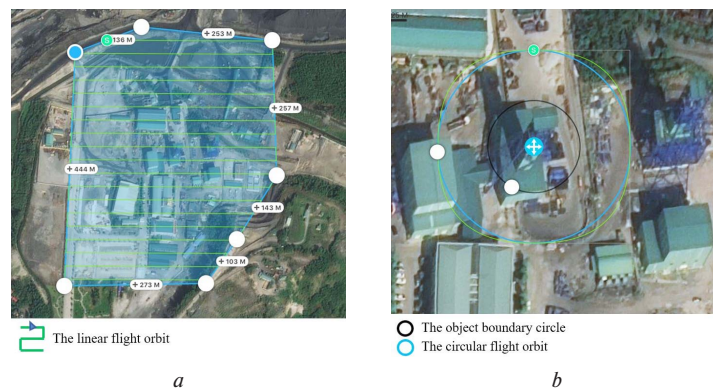


Fig. 5. Planning and performing:
a – the linear flight for the nadir image acquisition; b – the circular flight for the oblique image acquisition

Table 2

Flight plan parameters and UAV data

Flight modes	Flight height, (m)	Camera axis angle (degree)/radius, (m)	Image forward/side laps, (%)	Number of mission	Images	GSD, (cm)
Circular flights (O)	50–100	45/45	80/80	01	202	0.6
		30/45		01		
Linear flight (N)	100	0	75/75	01	125	2.7

mine shaft tower, such as roofs, could not be captured. However, many roofs of the surrounding buildings were sufficiently captured for the reference data used for the comparison of roofs (Fig. 6). The TLS point clouds of the ground surface, facades, roofs were used as the reference data to assess the quality of the entire 3D point clouds of these three objects, processed from the UAV imagery data.

Methodology. Fig 7 summarizes the study’s workflow which can be divided into three parts, including data acquisition, UAV and TLS data processing, and the quality assessment of point clouds. While the first part is described in sections 2.2 and 2.3, the others are presented in the following sections.

Structure from Motion (SfM) – photogrammetric processing. The SfM photogrammetry processing contains the following steps [21]: 1) Identification of keypoint features in images through the use of algorithms such as the Scale-Invariant

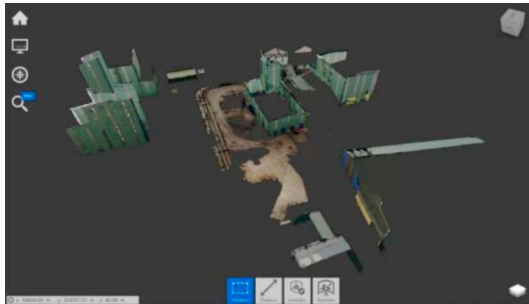


Fig. 6. TLS point clouds of the ground surfaces, roofs, and facades used for the accuracy assessment of UAV point clouds of these objects

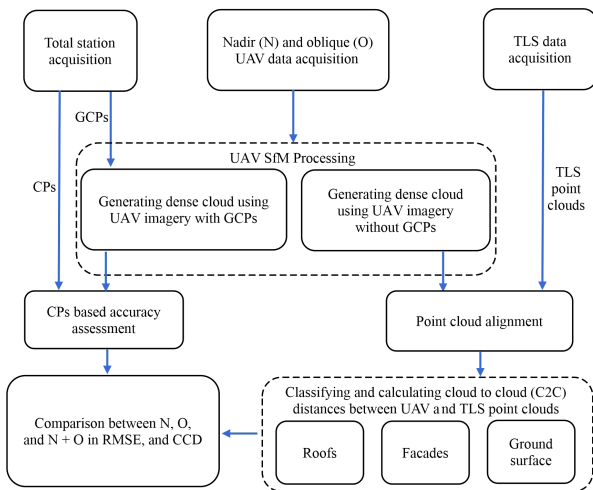


Fig. 7. Schematic workflow of quality assessment of UAV point clouds

Feature Transform (SIFT) [22]; 2) Images features matching; 3) Internal and external camera orientation; 4) Point cloud generation through dense image matching algorithms [23, 24].

In this study, the UAV SfM processing software was Agisoft Metashape (Agisoft LLC., St. Petersburg, Russia). Table 3 summarizes the computation parameters of the software. There were three scenarios of UAV dense cloud building, including the nadir (N) UAV, the oblique (O) UAV, and the nadir and oblique (N + O) UAV. Therefore, there would be three times processing these image blocks collectively.

In order to avoid any possible errors caused by GCP-based georeferencing to the accuracy of UAV and TLS point clouds, there was the case of no GCP in generating UAV and TLS point clouds. Therefore, the alignment of UAV and TLS point cloud is necessarily performed before classifying and extracting the UAV and TLS point clouds of ground surfaces, facades, and roofs. This work contains two steps, including coarse and fine alignments.

All TLS scans were processed and registered using the FARO Scene software before exporting their point clouds in the E57 format. The UAV and TLS point clouds in the E57 format were imported into the RECAP Pro software of AUTODESK to identify targets on facades and ground surfaces which in turn were used for the coarse alignment step. For the fine alignment, the algorithm of iterative closest point (ICP) [25] was used. The alignment was performed in the open-source software, CloudCompare.

Quality assessment of UAV point clouds. In this study, the quality refers to the accuracy and density of the UAV point clouds. Therefore, the quality assessment of the UAV point clouds includes the accuracy assessment and the calculation of point density. For the former, there were two accuracy assessment methods, including one based on CPs and another one based on cloud to cloud distances between UAV and TLS point clouds of ground surfaces, facades, and roofs.

Accuracy assessment based on CPs. In order to evaluate the accuracy of UAV point clouds generated by different flight configurations, including N, O, and combination of N and O, the Root Mean Square Error (RMSE) for X, Y, Z, X.Y., and XYZ were calculated, using the following equations

$$RMSE_X = \sqrt{\left(\frac{1}{n} \sum_{i=1}^n (X_{DSM} - X_{CPI})^2 \right)}$$

$$RMSE_Y = \sqrt{\left(\frac{1}{n} \sum_{i=1}^n (Y_{DSM} - Y_{CPI})^2 \right)}$$

$$RMSE_{XY} = \sqrt{RMSE_X^2 + RMSE_Y^2}$$

Table 3

Computation parameters of the software

Agisoft Metashape Workflow Align Photos	
Accuracy	High
Generic preselection	Enabled
Key point limit	40,000
Tie point limit	4000
Reference Settings	
Marker accuracy (m)	0.005
Marker accuracy (pix)	1
Tie point accuracy (pix)	2
Dense Cloud Building	
Quality	High
Depth filtering	Mild

Table 4

Results of CP based accuracy assessment

$$RMSE_Z = \sqrt{\left[\frac{1}{n} \sum_{i=1}^n (Z_{DSM} - Z_{CPi})^2 \right]}$$

$$RMSE_{XYZ} = \sqrt{RMSE_X^2 + RMSE_Y^2 + RMSE_Z^2},$$

where n is the number of CPs; X_{CPi} and X_{DSM} are the X -coordinate component of CPs and corresponding coordinate in Digital Surface Model (DSM), respectively; Y_{CPi} and Y_{DSM} are the Y -coordinate component of CPs and corresponding coordinate in DSM , respectively; Z_{CPi} and Z_{DSM} are the Z -coordinate component of CPs and corresponding coordinate in DSM , respectively.

Calculation of cloud – cloud (C2C) distances. Because of the much higher accuracy and density, the TLS point cloud was used as the reference data in this study. After aligning the UAV point clouds to the TLS one, the classification of both TLS and aligned UAV point clouds into ground surfaces, facades, and roofs were performed. At the next step, the cloud-to-cloud distances between classified UAV and TLS clouds were calculated. There are several computation methods such as nearest neighbour distance and local model-based distance. The former is simple as the system searches the closest reference point of each point in the compared cloud before calculating the Euclidean distance between this pair of points. If the reference point cloud is with a high density, this method can be used. However, if the reference point cloud is not dense enough, the nearest neighbour distance method might result in low accuracy. In this case, a model of reference surface is built by mathematically fitting it on the nearest point and several of its neighbours before computing the distance from the comparing point to this model. In this study, a high quadratic function was chosen as it is more precise than others, such as the least square fitting plane and $2D1/2$ Delaunay triangulation.

Point density decrease rate. In order to properly evaluate the effectiveness of each method, in addition to the CPs and cloud-cloud distance-based accuracy assessment methods, a point density decrease rate was used. With the assumption that all cloud points with the cloud-cloud distance of smaller than 0.1 m would be excluded, the point density decrease rate was calculated using the following formula

$$\Delta m = m_1 - m_2,$$

where Δm is the point density decrease rate; m_1 and m_2 are the cloud densities of pre-excluded and post-excluded point clouds. The point density decrease rate indicates that the bigger it is, the less precise the point cloud is.

Results and discussions. The UAV survey was completed with a total number of 327 images on a scale of 5472×3648 , including 125 nadir ones and 202 oblique ones. The TLS survey resulted in the data of eight scans. The two datasets were processed using the workflow in Fig. 9. UAV generated 6 600 186 points, 24 170 293 points, and 32 526 599 points for the Nadir (N), Oblique (O), and Nadir and Oblique (N + O) combination, respectively. TLS generated 172 684 627 points with the registration error of 8 mm. Table 4 summarizes the accuracy assessment of UAV point clouds, with three cases of N, O, and N + O.

Table 4 reports that the number of CPs used for the accuracy assessment is different between the three study cases. Case N used seven CPs and resulted in RMSEs of X , Y , $X.Y.$, and Z , and XYZ equalling 2.4, 3.0, 3.9, 3.8 and 5.5 cm, respectively. Case O used just four CPs, and RMSEs of X , Y , $X.Y.$, and Z , and XYZ equalling 1.7, 6.1, 6.4, 3.0 and 7.0 cm, respectively. Case N+O used the biggest number of nine CPs, and RMSEs of X , Y , $X.Y.$, and Z , and XYZ equalling 2.7, 4.1, 4.9, 4.6 and 6.7 cm, respectively. By comparison in RMSEs of $X.Y.$ (the positional accuracy), the results demonstrated that Case N was the most accurate one, followed by Case N + O, and Case O. However, by comparison in RMSEs of Z (the vertical

Cases	CPs	Error, cm				
		X	Y	XY	Z	XYZ
Nadir	T1	3.3	-1.9	3.8	-1.9	4.2
	9	-3.2	-2.2	3.9	-0.4	3.9
	23	-2.3	-0.9	2.5	-3.8	4.6
	15	-0.4	-6.1	6.1	2.0	6.4
	14	2.6	-3.9	4.7	9.2	10.3
	T5	2.2	-1.2	2.5	-0.6	2.6
	T8	1.1	-0.4	1.1	0.1	1.1
	RMSE	2.4	3.0	3.8	3.9	5.5
Oblique	A013	-0.1	8.5	8.5	0.3	8.5
	T14.1	2.6	7.4	7.9	-2.2	8.2
	T5	-1.9	-4.7	5.0	-4.9	7.0
	T8	-1.1	-1.3	1.7	-2.7	3.2
	RMSE	1.7	6.1	6.4	3.0	7.0
Nadir + Oblique	T1	4.1	-3.6	5.5	-3.5	6.5
	9	-3.2	-1.9	3.8	-0.8	3.9
	23	-2.1	-0.5	2.2	-4.4	4.9
	14	3.2	-3.6	4.8	11.7	12.7
	15	0.0	-5.6	5.6	3.1	6.4
	A013	-3.4	7.6	8.3	1.2	8.4
	T14.1	-0.5	3.5	3.6	-0.3	3.6
	T5	3.0	-3.4	4.5	-2.5	5.2
	T8	1.7	-2.8	3.3	-1.0	3.5
RMSE	2.7	4.1	4.9	4.6	6.7	

accuracy), Case O was the most accurate one, followed by Case N, and Case N + O.

However, the difference between the number of CPs among the three cases might not be compatible with the above comparisons. Therefore, if using two common CPs, namely T5 and T8, it can be seen that Case N was the most accurate in both vertical (Z) and horizontal dimensions ($X.Y.$). When making a comparison between Case O and Case N+O, two more CPs placed on the elevated parts of the mine shaft tower were used. The results showed that Case N + O were more accurate than Case O, with RMSEs of 5.3 and 6.3 cm in the horizontal dimension ($X.Y.$), and RMSEs of 1.4 and 3.0 cm in the vertical dimension (Z), respectively.

In the next step, comparisons between the UAV photogrammetric point clouds and the TLS reference one were performed by Cloudcompare software. For this purpose, the UAV clouds were registered to the TLS one using the ICP algorithm. This process resulted in the registered UAV clouds with an accuracy of approximately 0.04 m. The classification was conducted of UAV and TLS point clouds into three objects, including ground surfaces, facades, and roofs. Each sub-cloud of these objects extracted from Cases N, O, and N + O was used as the compared cloud of comparisons.

Fig. 8 represents the histograms of C2C distances with the Gauss distribution and the C2C distance maps on the three objects, including ground surfaces, facades, and roofs. Maps provide a global view of the discrepancy between the two sub-clouds and highlight the deviations in the different areas of the object between them, while histograms with the Gauss distribution offer statistic parameters, including mean and standard deviations.

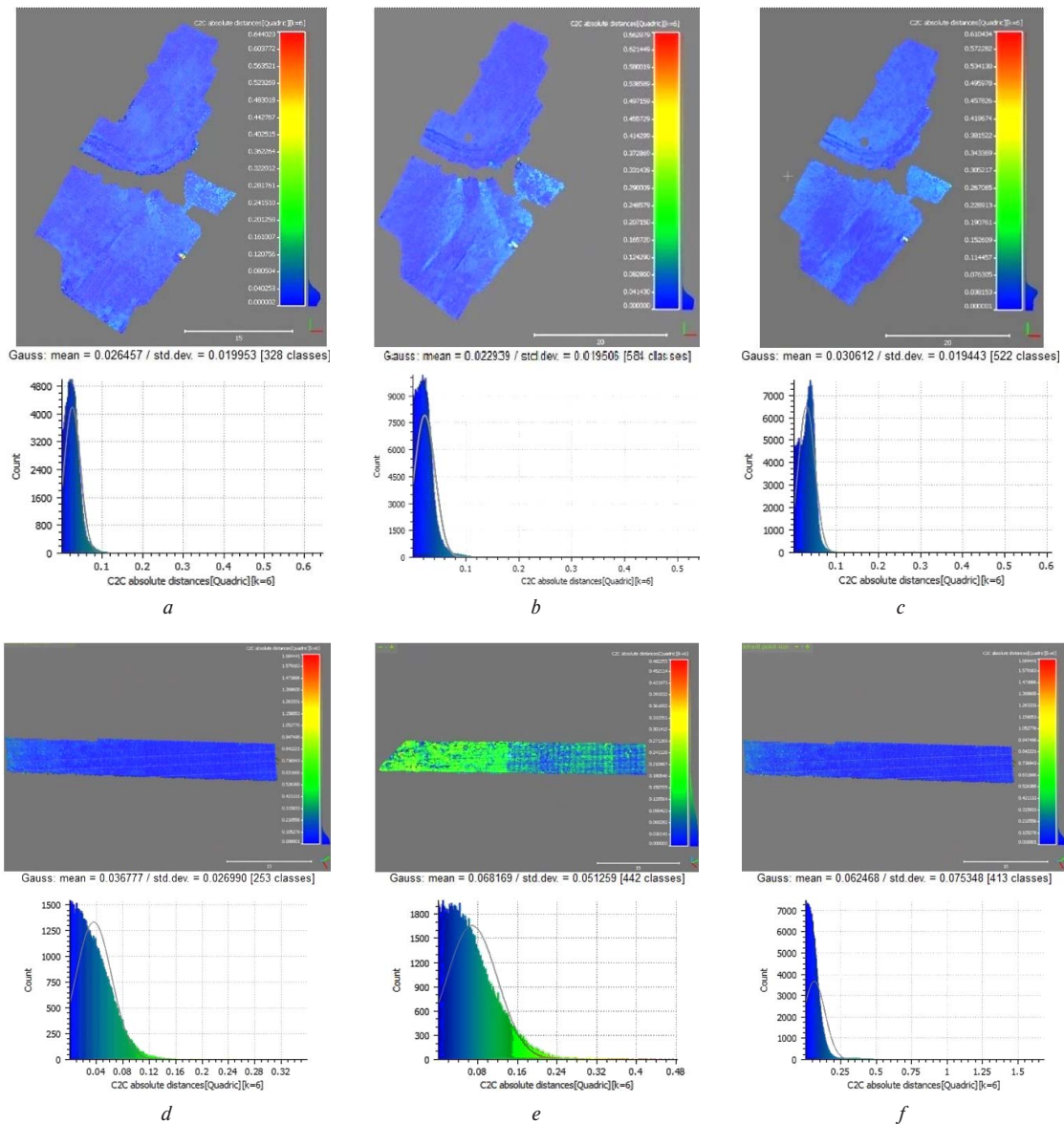


Fig. 8. C2C distance histograms with Gauss distribution and C2C distance maps of three objects: ground surfaces from Case: a – Nadir (NG); b – Oblique (OG); c – Nadir-Oblique (NOG); d – Nadir (NR); e – Oblique (OR); f – Nadir-Oblique (NOR)

1. Comparison between three objects.

It is observed from Fig. 9 that in all three cases, the facades had the biggest standard deviation (an average value of 0.279 m), followed by the roofs with an average of 0.050 m, whereas the ground surfaces had the lowest standard deviation (0.019 m). Also, the maps in Fig. 10 illustrate that there is a good congruence between the sub-clouds on ground surfaces and roofs. For the facades, under close scrutiny, the major discrepancies occur in the lower parts of the facades.

2. Comparison between three cases N, O, and N + O.

For the ground surfaces, it is observed that all three cases produced a standard deviation of 0.019 m, but Case N had a slightly bigger mean than Case O, and Case N + O produced the biggest mean of 0.031 m. For the roofs, Case N + O had the biggest standard deviation, followed by Case O and N, with the standard deviations of 0.075, 0.051, and 0.026 m, respectively. Six facades were investigated for Cases O and N + O as Case N produced very poor point clouds. The reason for large gaps on the point cloud of facades from Case N was probably lower image coverage on the facades when the drone flew with the single flight direction pattern. Fig. 9 shows that the standard deviations of six facade sub-clouds ranged from 0.155 to 0.484 m and from 0.122 to 0.444 m for Case O and N + O, respectively.

Table 5 reports that Case O has the highest density of points, followed by Cases N + O and N. This is because Case O captured images with the highest resolution, a GSD of 0.6 cm, whereas that of Case N was 2.7 cm. For Case O, the facades have the highest point density, followed by the roofs and the ground surfaces, with 8.8, 6.5 and 6.3 points per dm², respectively. With Case N, the point density drastically decreased to 2.3, 2.1 and 1.8 points/dm² for the ground surfaces, roofs, and facades, respectively. Case N + O generated a point density that was slightly lower than that of Case O but significantly higher than that of Case N, with a cloud density of 5.9 points per dm² for the facades and 5.6 points per dm² for both the ground surfaces and roofs. Besides, it can be seen that from the ground to the top, while Cases O and N + O showed an upward trend in the cloud density, Case N had an opposite trend.

In term of the density decrease rate, Table 6 shows that Case N produced point clouds with the best accuracy as the average density decrease rate ranges from 0 to 1 point/dm². Case O generated point clouds with the lowest accuracy because their average cloud density decrease rate of point clouds was between 0.1 and 7.1 points/dm², while the point clouds from Case N + O had a rate ranging from 0 to 4.7 points/dm². In a comparison between the three objects, it can be seen that

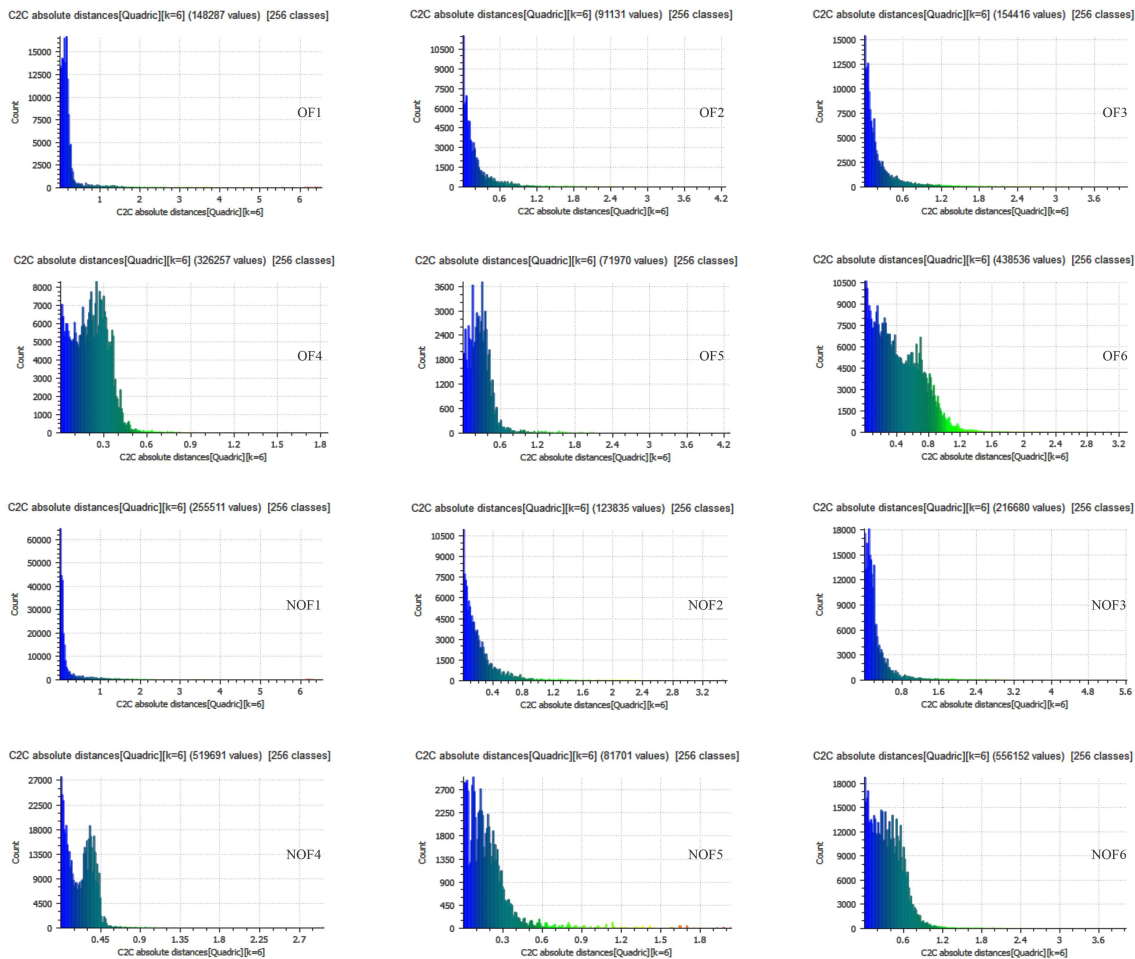


Fig. 9. C2C distance histograms with Gauss distribution of six facades from Case Oblique (OF) and Case Nadir-Oblique (NOF)

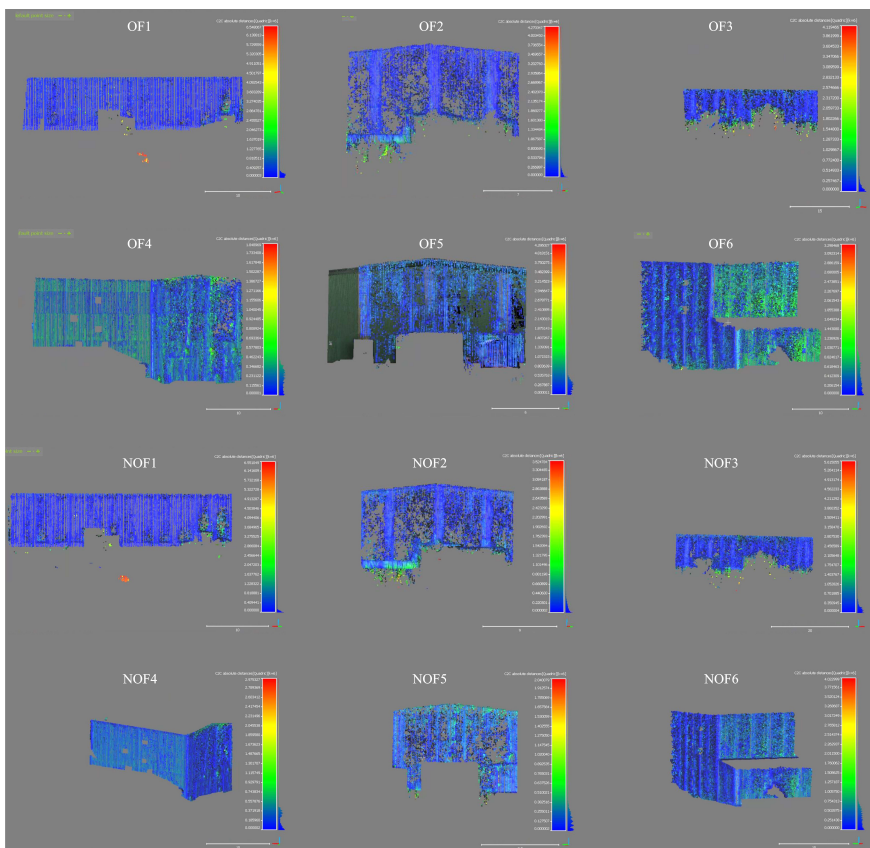


Fig. 10. C2C distance maps of six facades from Case Oblique (OF) and Case Nadir-Oblique (NOF)

Table 5

Average cloud density of point clouds

Objects	Mean cloud density (points/dm ²)		
	Case N	Case O	Case N + O
Ground	2.3	6.3	5.6
Roof	2.1	6.5	5.6
Facade	1.8	8.8	5.9

Table 6

Average cloud density decrease rate of point clouds

No	Cases Objects	Mean cloud density decrease rate (points/dm ²)		
		N	O	N + O
1	Ground	0	0.1	0
2	Roof	0.4	2.5	1.8
3	Facade	1.0	7.1	4.7

the ground surfaces had the lowest rate and the facades had the largest rate in all three cases. The largest rate is 7.1 points/dm² for the facades found in Case O.

Conclusions. This paper presents the quality assessment of 3D modeling of industrial buildings generated by the UAV photogrammetry method. Two UAV flight modes, including the linear and circular flights, were performed for capturing the nadir and oblique images, respectively. There were three study cases regarding the type of UAV images, including Case N using the nadir dataset, Case O using the oblique dataset, and Case N + O using both nadir and oblique datasets. In each case, the imagery dataset was used for generating point clouds with the UAV-SfM workflow. The point cloud model of three main objects, namely ground surfaces, facades, and roofs, were examined in their accuracy and point density. For the accuracy assessment, CPs measured by a total station and the TLS point clouds were used as the reference data. While CPs coordinates were used to compute RMSEs, C2C distances between UAV and TLS clouds described in standard deviations and means, as well as the point density decrease rate, were used for a more detailed analysis of cloud precision. The study arrives at the following conclusions:

Case N produces the most accurate but the least dense point clouds with large gaps on facades, so it is not suitable for recording features exposed along vertical facades. This conclusion confirms comments found in [12, 26, 27].

The oblique generates point clouds with the highest level of density but the lowest accuracy compared to the nadir and combined cases, especially regarding the facades.

When combining the dataset of both flight modes, the generated point clouds take advantage of individual mode. Specifically, the point cloud's accuracy is higher than that of Case O, and its density is much higher than that of Case N.

The point clouds of ground surfaces and roofs have a good congruence, while opposition is seen in those of facades.

In general, an approach of combining the nadir and oblique imagery is optimal to build exceptional accurate and dense point clouds of buildings.

Acknowledgements. Funding for this project was provided by the Hanoi University of Mining and Geology within the project: T21-19.

References.

1. Cilek, A., Donmez, C., & Ünal, M. (2020). Generation of High-Resolution 3-D Maps for Landscape Planning and Design Using UAV Technologies. *Journal of Digital Landscape Architecture*, 5(1), 275-284.

2. La, H.P. (2019). Web-based visualization of 3D city model using open source tools for urban planning (in Vietnamese). *Journal of Mining and Earth Sciences*, 60(2), 77-87.
3. Kalinichenko, V., Dolgikh, O., Dolgikh, L., & Pysmennyi, S. (2020). Choosing a camera for mine surveying of mining enterprise facilities using unmanned aerial vehicles. *Mining of Mineral Deposits*, 14(4), 31-39. <https://doi.org/10.33271/mining14.04.031>.
4. Urech, P.R.W., Dissegna, M.A., Girot, C., & Grêt-Regamey, A. (2020). Point cloud modeling as a bridge between landscape design and planning. *Landscape and Urban Planning*, 203, 103903. <https://doi.org/10.1016/j.landurbplan.2020.103903>.
5. Van Canh, L., Xuan Cuong, C., Quoc Long, N., Thi Thu Ha, L., Trung Anh, T., & Bui, X.N. (2020). Experimental Investigation on the Performance of DJI Phantom 4 RTK in the PPK Mode for 3D Mapping Open-Pit Mines. *Inżynieria Mineralna*, 1(2), 65-74. <https://doi.org/10.29227/IM-2020-02-10>.
6. Long, N., Nam, B., Cuong, C., & Canh, L. (2019). An approach of mapping quarries in Vietnam using low-cost Unmanned Aerial Vehicles. *Sustainable Development of Mountain Territories*, 11(2), 199-210. <https://doi.org/10.21177/1998-4502-2019-11-2-199-210>.
7. Long, N.Q., Buczek, M.M., Hien, L.P., Szlapińska, S.A., Nam, B.X., Nghia, N.V., & Cuong, C.X. (2018). Accuracy assessment of mine walls' surface models derived from terrestrial laser scanning. *International Journal of Coal Science & Technology*, 5(3), 328-338. <https://doi.org/10.1007/s40789-018-0218-1>.
8. Nguyen, L.Q. (2021). Accuracy assessment of open - pit mine's digital surface models generated using photos captured by Unmanned Aerial Vehicles in the post - processing kinematic mode. *Journal of Mining and Earth Sciences*, 62(4), 38-47. [https://doi.org/10.46326/JMES.2021.62\(4\).05](https://doi.org/10.46326/JMES.2021.62(4).05).
9. Nguyen, Q.L., Le, T.T.H., Tong, S.S., & Kim, T.T.H. (2020). UAV Photogrammetry-Based For Open Pit Coal Mine Large Scale Mapping, Case Studies In Cam Pha City, Vietnam. *Sustainable Development of Mountain Territories*, 12(4), 501-509. <https://doi.org/10.21177/1998-4502-2020-12-4-501-509>.
10. Nguyen, Q.L., Ropesh, G., Bui, K.L., Le, V.C., Cao, X.C., Pham, V.C., Bui, N.Q., & Xuan-Nam, B. (2020). Influence of Flight Height on the Accuracy of UAV Derived Digital Elevation Model at Complex Terrain. *Inżynieria Mineralna*, 1(45), 179-186. <https://doi.org/10.29227/IM-2020-01-27>.
11. Nguyen, Q.L., Ropesh, G., Bui, K.L., Cao, X.C., Le, V.C., Nguyen, Q.M., & Xuan-Nam, B. (2021). Optimal Choice of the Number of Ground Control Points for Developing Precise DSM Using Light-Weight UAV in Small and Medium-Sized Open-Pit Mine. *Archives of Mining Sciences*, 66(3), 369-384. <https://doi.org/10.24425/ams.2021.138594>.
12. Nesbit, P.R., & Hugenholtz, C.H. (2019). Enhancing UAV-SfM 3D Model Accuracy in High-Relief Landscapes by Incorporating Oblique Images. *Remote Sensing*, 11(3), 239. <https://doi.org/10.3390/rs11030239>.
13. Vacca, G., Dessì, A., & Sacco, A. (2017). The Use of Nadir and Oblique UAV Images for Building Knowledge. *ISPRS International Journal of Geo-Information*, 6(12), 393. <https://doi.org/10.3390/ijgi6120393>.
14. Aicardi, I., Chiabrando, F., Grasso, N., Lingua, A.M., Noardo, F., & Spanò, A. (2016). UAV photogrammetry with oblique images: first analysis on data acquisition and processing. *International archives of the photogrammetry, remote sensing and spatial information sciences*, XLI-B1, 835-842. <https://doi.org/10.5194/isprsarchives-xli-b1-835-2016>.
15. Bemis, S.P., Micklethwaite, S., Turner, D., James, M.R., Akciz, S., Thiele, S.T., & Bangash, H.A. (2014). Ground-based and UAV-Based photogrammetry: A multi-scale, high-resolution mapping tool for structural geology and paleoseismology. *Journal of Structural Geology*, 69, 163-178. <https://doi.org/10.1016/j.jsg.2014.10.007>.
16. Markelin, L., Honkavaara, E., Näsi, R., Nurminen, K., & Hakala, T. (2014). Geometric processing workflow for vertical and oblique hyperspectral frame images collected using UAV. *International archives of the photogrammetry, remote sensing and spatial information sciences*, XL-3, 205-210. <https://doi.org/10.5194/isprsarchives-xl-3-205-2014>.
17. Harwin, S., Lucieer, A., & Osborn, J. (2015). The Impact of the Calibration Method on the Accuracy of Point Clouds Derived Using Unmanned Aerial Vehicle Multi-View Stereopsis. *Remote Sensing*, 7(9), 11933-11953. <https://doi.org/10.3390/rs70911933>.
18. Lingua, A., Noardo, F., Spanò, A., Sanna, S., & Matrone, F. (2017). 3D model generation using oblique images acquired by UAV. *The International Archives of the Photogrammetry, Remote Sensing and Spatial Information Sciences*, XLII-4/W2, 107-115. <https://doi.org/10.5194/isprs-archives-xlii-4-w2-107-2017>.

19. Russo, M., Carnevali, L., Russo, V., Savastano, D., & Taddia, Y. (2019). Modeling and deterioration mapping of façades in historical urban context by close-range ultra-lightweight UAVs photogrammetry. *International journal of architectural heritage*, 13(4), 549-568. <https://doi.org/10.1080/15583058.2018.1440030>.
20. Pepe, M., Fregonese, L., & Crocetto, N. (2019). Use of SfM-MVS approach to nadir and oblique images generated through aerial cameras to build 2.5D map and 3D models in urban areas. *Geocarto International*, 1-22. <https://doi.org/10.1080/10106049.2019.1700558>.
21. Marcisz, M., Proberz, K., & Ostrowska-Łach, M. (2018). 3D representation of geological observations in underground mine workings of the Upper Silesian Coal Basin. *Journal of Sustainable Mining*, 17(1), 34-39. <https://doi.org/10.1016/j.jsm.2018.01.001>.
22. Lowe, D.G. (2004). Distinctive Image Features from Scale-Invariant Keypoints. *International Journal of Computer Vision*, 60(2), 1-110. <https://doi.org/10.1023/B:VISI.0000029664.99615.94>.
23. Furukawa, Y., & Ponce, J. (2010). Accurate, Dense, and Robust Multiview Stereopsis. *IEEE Transactions on Pattern Analysis and Machine Intelligence*, 32(8), 1362-1376. <https://doi.org/10.1109/TPAMI.2009.161>.
24. Furukawa, Y., Curless, B., Seitz, S. M., & Szeliski, R. (2010). Towards Internet-scale multi-view stereo. *IEEE Computer Society Conference on Computer Vision and Pattern Recognition*, 1434-1441. <https://doi.org/10.1109/CVPR.2010.5539802>.
25. Shi, X., Liu, T., & Han, X. (2020). Improved Iterative Closest Point (ICP) 3D point cloud registration algorithm based on point cloud filtering and adaptive fireworks for coarse registration. *International Journal of Remote Sensing*, 41(8), 3197-3220. <https://doi.org/10.1080/01431161.2019.1701211>.
26. Rossi, P., Mancini, F., Dubbini, M., Mazzone, F., & Capra, A. (2017). Combining nadir and oblique UAV imagery to reconstruct quarry topography: methodology and feasibility analysis. *European Journal of Remote Sensing*, 50(1), 211-221. <https://doi.org/10.1080/22797254.2017.1313097>.
27. Rittersbacher, A., Buckley, S.J., Howell, J.A., Hampson, G.J., & Vallet, J. (2014). Helicopter-based laser scanning: a method for quantitative analysis of large-scale sedimentary architecture. *Geological Society, London*, 185-202. <https://doi.org/http://dx.doi.org/10.1144/SP387.3/>.

Оцінка якості тривимірної хмари точок промислових будівель на основі зображень планової та перспективної зйомки БПЛА

Као Суан Куонг¹, Ле Ван Кань¹, Фам Ван Тьонг¹,
Ле Дук Тінг¹, Фам Трунг Дунг¹, Нго Су Куонг²

1 – Ханойський університет гірничої справи та геології, м. Ханой, Соціалістична Республіка В'єтнам, e-mail: caoxuancuong@humi.edu.vn

2 – Корпорація природних ресурсів і навколишнього середовища В'єтнаму, м. Ханой, Соціалістична Республіка В'єтнам

Мета. Основна мета даної роботи – оцінити якість 3D-моделі промислових будівель, створеної на основі ряду даних безпілотних літальних апаратів (БПЛА), включаючи дані БПЛА у плановій зйомці (надир (Н)), у перспективній зйомці (П), а також у плановій і перспективній зйомці (Н + П).

Методика. Якість 3D-моделі визначається точністю та щільністю хмар точок, створених на основі зображень БПЛА. Із цією метою БПЛА був розгорнутий для отримання зображень у режимах польоту як планової, так і перспективної зйомки над промисловим районом видобутку корисних копалин, що містить вежу шахти, заводські корпуси та офісні будівлі. Оцінка якості проводилася для тривимірної моделі хмари точок трьох основних об'єктів, таких як дахи, фасади й поверхні землі, з використанням хмар контрольних точок (КТ) і наземного лазерного сканування (НЛС) в якості еталонних наборів даних. Середньоквадратичне похибки (СКП) були розраховані з використанням координат КТ, а відстані від хмари до хмари були розраховані з використанням хмар точок НЛС, що застосовувалися для оцінки точності.

Результати. Результати показали, що модель хмари точок, створена в режимі польоту Н, була найбільш точною, але найменш щільною, тоді як модель у режимі П показала найменш точний, але найбільш деталізований рівень у порівнянні з іншими. Крім того, комбінація наборів даних П і Н дає переваги окремого режиму, оскільки точність хмари точок вище, ніж у разі П, а його щільність набагато вище, ніж у разі Н. Отже, вона оптимальна для створення виключно точних і щільних хмар точок будівель.

Наукова новизна. У роботі проводиться порівняльний аналіз якості хмари точок дахів і фасадів, створеного за допомогою фотограмметрії БПЛА для виробничих будівель гірничої промисловості.

Практична значимість. Результати дослідження можуть бути використані в якості довідкових матеріалів як для практики дослідження БПЛА, так і для додатків хмари точок БПЛА. У роботі представлена корисна інформація для планування польотів БПЛА, або того, які точки БПЛА слід інтегрувати в точки НЛС для отримання найкращої хмари точок.

Ключові слова: БПЛА, перспективний, надир, 3D-моделювання, наземне лазерне сканування, оцінка якості

Recommended for publication by Dr. Nguyen Quoc Long. The manuscript was submitted 17.04.21.